Nature Nanotechnology
NNANO-19010113B
Final version

SUBRETINALLY INJECTED SEMICONDUCTING POLYMER NANOPARTICLES RESCUE VISION IN A RAT MODEL OF RETINAL DYSTROPHY

José Fernando Maya-Vetencourt[1,2,3], Giovanni Manfredi[4], Maurizio Mete[5], Elisabetta Colombo[1,2], Mattia Bramini[1]*, Stefano Di Marco[1,2], Dmytro Shmal[1], Giulia Mantero[1], Michele Dipalo[6], Anna Rocchi[1,2], Mattia L. DiFrancesco[1], Ermanno D. Papaleo[1], Angela Russo[5], Jonathan Barsotti[4], Cyril Eleftheriou[1]^, Francesca Di Maria[7], Vanessa Cossu[2,8], Fabio Piazza[9], Laura Emionite[2], Flavia Ticconi[2,8], Cecilia Marini[10], Gianmario Sambuceti[2,8], Grazia Pertile[5], Guglielmo Lanzani[4,11], Fabio Benfenati[1,2]

[1]Centre for Synaptic Neuroscience and Technology, Istituto Italiano di Tecnologia, Genoa, Italy; [2]IRCCS Ospedale Policlinico San Martino, Genoa, Italy; [3]Department of Biology, University of Pisa, Pisa, Italy; [4]Centre for Nano Science and Technology, Istituto Italiano di Tecnologia, Milan, Italy; [5]Ophthalmology Department, Sacro Cuore Hospital - Don Calabria, Negrar, Italy; [6]Plasmon Nanotechnologies, Istituto Italiano di Tecnologia, Genoa, Italy; [7]CNR Institute of Organic Synthesis and Photoreactivity (ISOF), Bologna, Italy; [8]Department of Health Science, Nuclear Medicine, University of Genoa, Genoa, Italy; [9]ENT Department, ASST Mantova, Mantua, Italy; [10]CNR Institute of Bioimages and Molecular Physiology, Milan (Genoa section), Italy; [11]Department of Physics, Politecnico di Milano, Milan, Italy.

*Present address: Department of Applied Physics, University of Granada, Granada, Spain.
^Present address: Departments of Ophthalmology and Neurology, Weil Medical College of Cornell University, White Plains, NY, USA.

Corresponding authors:
Fabio Benfenati, MD, Centre for Synaptic Neuroscience and Technology, Istituto Italiano di Tecnologia. email: fabio.benfenati@iit.it
Guglielmo Lanzani, PhD, Centre for Nano Science and Technology, Istituto Italiano di Tecnologia. email: guglielmo.lanzani@iit.it

ABSTRACT

Inherited retinal dystrophies and late-stage age-related macular degeneration are among the most prevalent causes of legal blindness, for which treatments remain limited. Retinal prostheses have been developed to stimulate the inner retinal network; however, lack of sensitivity and resolution, and the need for wiring or external cameras have limited their application. Here we show that conjugated polymer nanoparticles (P3HT-NPs) mediate light evoked stimulation of retinal neurons and persistently rescue visual functions when injected subretinally in a rat model of *Retinitis Pigmentosa* (RP). P3HT-NPs spread out over the entire subretinal space and promote light-dependent activation of spared retinal neurons, recovering subcortical, cortical and behavioural visual responses in the absence of retinal inflammation or trophic effects. By conferring sustained light-sensitivity to degenerate retinas after a single injection, and with the potential for high spatial resolution, P3HT-NPs provide a new avenue in retinal prosthetics with potential applications not only in RP, but also in age-related macular degeneration.

Short title: P3HT nanoparticles rescue degenerative blindness

Keywords: photoexcitation, conjugated polymers, photoreceptor degeneration, retinal prosthesis, visual rescue

Website Summary

Semiconducting polymer nanoparticles can act as light-sensitive interfaces with retinal neurons, and upon micoroinjection in the eye, rescue vision in retinas affected by photoreceptor degeneration, offering a potential new treatment option for inherited retinal dystrophies and late-stage age-related macular degeneration.

The progressive degeneration of retinal photoreceptors is one of the most frequent causes of severe visual impairment in developed and aging populations. The two most prevalent retinal degenerative diseases are age-related macular degeneration (AMD), and Retinitis Pigmentosa (RP) [1]. RP, a collective name for a set of genetic disorders that cause death of rods and secondarily of cones, afflicts 1 in 4,000 people worldwide and is the most common inherited retinal degeneration, while the atrophic form of AMD affects about 1.4-20% of the population between 70 and 90 years worldwide and primarily targets foveal cones [2]. Gene supplementation, optogenetic or stem cell therapies for these diseases are very promising but, except for the first commercially available gene therapy for RPE65-linked retinal dystrophies, are still in preclinical experimentation or early phases of human testing [3-5]. Thus, several groups have tried to rescue vision by electrically stimulating the substantially preserved inner retinal circuits with epiretinal, subretinal or suprachoroidal prosthetic implants [6-11].

Organic semiconductors have been introduced as interfaces for neuronal photo-stimulation in retinal prostheses [12,13]. In such devices, a conjugated polymer (CP; such as poly[3-hexylthiophene], P3HT) layer is contacting on the one side an underlying conductive layer (ITO or PEDOT:PSS) and bathed, on the opposite side, by the electrolytic extracellular medium [14-17]. When such a device, layered onto a silk fibroin support, was implanted in the subretinal space of dystrophic Royal College of Surgeons (RCS) rats, a widely recognized model of RP [18], it promoted a persistent CP-dependent rescue of vision that lasted up to 6-10 months after implantation with sensitivity in the daylight range and high biocompatibility [19-22].

High-resolution sampling of retinal images relies on the mosaic of foveal cones of about 4-5 µm in diameter that generate the dedicated midget system and provide the vast majority of the input to the visual cortex [23]. However, all the existing 2D prosthetic approaches achieve a spatial resolution over one order of magnitude lower that the one allowed by foveal cones. To circumvent these problems, we exploited the huge potential of multifunctional nanoscale materials [24-27]. We engineered P3HT nanoparticles (P3HT-NPs) [28,29] as light-sensitive interfaces with retinal neurons. We find that P3HT-NPs of ≈300 nm in diameter remain extracellular and endow neurons in blind retinal explants with light sensitivity. When microinjected in the eye of RCS rats, P3HT-NPs widely and persistently distribute in the whole subretinal space in the absence of trophic effects on residual photoreceptors or significant inflammatory reactions and rescue light-driven behaviours, visual cortex activity and visual acuity to levels indistinguishable from healthy congenic rats for up to 8 months after a single injection. The results indicate that P3HT-NPs represent a promising approach to the treatment of both RP and AMD for both the low invasive surgery procedure, the permanence of the effects and the potential for high spatial resolution to be exploited in high-acuity models.

Photostimulation of retinal neurons by P3HT-NPs

To ascertain whether the conductive layer in the planar organic prosthesis is needed to elicit *in vivo* effects, we fabricated a planar device in which P3HT was directly layered onto a passive polyethylene terephthalate (PET) substrate and implanted it in the subretinal space of RCS rats. P3HT-implanted animals showed a significant increase in the amplitude of visually evoked potentials (VEPs) in the primary visual cortex (V1) 30 days after surgery with respect to sham-operated RCS rats (**Supplementary Fig.1**), demonstrating that the photoactive polymer directly mediates the bio-stimulation. Thus, we proceeded to generate P3HT-NPs following recently reported procedures [28,29].

Sterile P3HT-NPs were prepared using the re-precipitation technique and sorted by differential centrifugation and size-matched glass-NPs were used as control (sham). The shape of P3HT-NPs, analysed by scanning electron microscopy (SEM; **Fig.1a**), ranged from spherical to elliptic and their size distribution assessed by dynamic light scattering (DLS) overlapped with that of the more homogeneous spherical glass-NPs (Z-average = 304 nm *vs* 254 nm of glass-NPs with low dispersity indexes (**Supplementary Fig.2**). Next, we verified that P3HT-NPs were not endocytosed by neurons. Indeed, P3HT-NPs displayed a very low degree of colocalization with the lysosome-specific marker LAMP1 up to 7 d of incubation and fine decorated the neuronal membrane all along the processes, positioning them at the very site of action for neurostimulation (**Extended Data Fig.1**). Confocal fluorescence microscopy, SEM and cross-section SEM on primary neurons plated onto a drop-casted layer of P3HT-NPs indeed showed that neurons engulfed NPs without internalizing them, thus creating an intimate contact between the NP surface and the neuronal membrane, with a quasi-virtual (< 20 nm) cleft secluded from the extracellular fluid (**Fig.1b**).

We tested the ability of the NP-membrane interface to induce light-dependent neuronal activation in blind retina explants from 12-14 months-old RCS rats. Patch-clamped RGCs puffed with P3HT-NPs and exposed to light stimuli (40mW/mm^2;500ms) displayed a robust depolarization time-locked with the light stimulus, followed by deterministic firing (**Fig.1c,d**). To mimic *in vivo* experiments, we next microinjected P3HT-NPs in the subretinal space of blind retina explants from over 12-14 months-old RCS rats. P3HT-NPs triggered a light-dependent RGC firing that was completely absent from glass NP-injected retinas (**Fig.1e**). P3HT-NP induced firing was characterized by a longer latency (≈300 ms) with respect to age-matched healthy retinal explants (**Fig.1f**), likely due to the marked rewiring of the aged RCS retinas [30] and consistent with the *in vivo* latencies of V1 cortical responses to light (see below).

Photoinduced heating can contribute to photostimulation at high powers and under conditions of limited heat dissipation (such as with P3HT films; [15,31]). However, simulations of P3HT-NPs dispersed in water under the conditions used for the experiments indicate a negligible temperature increase in the mK range (**Supplementary Text**). Alternatively, it has been

demonstrated that, upon photoexcitation, negative charges are generated at the polymer/electrolyte surface [14,16,32]. The amount of charge that can be accumulated is in the order of nC/cm^2. Considering the low area coverage of NPs in *ex-vivo* experiments (5 10^5 NPs/cm^2;**Supplementary Text**), the generated current is around μA/cm^2, orders of magnitude lower than the values needed to open voltage-dependent conductances [12]. We also demonstrated the lack of significant increases in the local concentration of cations such as H^+ and Na^+, since no significant light-dependent changes in heat and pH-sensitive TRPV1 and ASIC1a currents or in the cell volume were observed in HEK293 cells plated onto P3HT-NPs (**Supplementary Figs.3,4**). Moreover, the light-induced firing activation in blind retina explants was unaffected by blockers of TRPV or ASIC1a channels (**Supplementary Fig.5**). Given these negative results, we considered the capacitive mechanism that relies on the close contact between NPs and the very high electrical resistance of the cleft, reminiscent of what found for mushroom-shaped electrodes [33,34] or nanopillars [35]. We designed a model to capture the NP-cell coupling assuming the experimentally determined cleft maximum thickness of 20 nm (**Fig.1g**; **Table S1** and **Supplementary Text** for a complete description). We found that a junctional membrane resistance > 1 MΩ is associated with a change in membrane potential > 1 mV. (**Fig.1h**). Such small photo-potentials that, similar to postsynaptic potentials in central synapses, are evoked in adjacent sites and repeated in time, will summate both spatially and temporally to build up a significant depolarization.

Subretinal P3HT-NPs do not trigger trophic or proinflammatory effects

Suspensions of P3HT-NPs were bilaterally injected in the subretinal space through a 38-gauge needle inserted tangentially in the superior-temporal quadrant (**Fig.2a**). The transient retinal detachment was confirmed by ophthalmoscopy immediately after the procedure. *In vivo* OCT 30 and 240 days post-injection (DPI) confirmed the absence of retinal lesions or detachments indicating that the retina spontaneously reattached to the choroid thanks to the osmotic pumping of the retinal pigment epithelium (**Supplementary Fig.6**).

Both P3HT-NPs and fluorescent glass-NPs remained confined to the outer retina, in place of degenerated photoreceptors, while they tangentially diffused from the injection site to cover most of the subretinal space (**Fig.2a,b**). Morphometric analysis of z-stack confocal images revealed that both P3HT-NPs and fluorescent glass-NPs were organized in clusters of closely similar size distribution in ventral, central and dorsal retina, with the highest frequency at a volume of 10 μm^3 and an overall coverage of about 80% (**Fig.2a,b**;**Supplementary Fig.7**). Subretinal NPs can be in principle cleared by microglia or by the choroid circulation over time. However, we found a full persistence of P3HT-NPs at 240 DPI, with only minor changes in their cluster size distribution with respect to 30 DPI (**Fig.2c**).

It has been reported that surgical manipulations of the retina in the pigmented RCS rats can lead

to an increased survival of degenerating photoreceptors [36-39]. Thus, we investigated whether the injection of either P3HT- or glass-NPs non-specifically enhanced photoreceptor survival in our 3 months-old pink-eyed albino RCS rats. We first analysed the thickness of the avascular outer nuclear layer (ONL) at both 30 and 240 DPI by staining retinal and choroidal vessels. At 30 DPI, the outer retina of RCS rats already displayed a complete derangement with markedly decreased thickness, invasion by retinal vessels and broadening of the INL. These changes were independent of whether the RCS rats had been non-injected or injected with either P3HT- or glass NPs and confirm the fast photoreceptor degeneration reported in this RCS strain at the same age [40]. A qualitatively similar, but more severe, picture was observed in 240 DPI retinas, in which the ONL was virtually absent. Counting of the cell body rows revealed that virtually all RCS retinas at 30 DPI had a greatly (80-85%) decreased number of cell rows in the ONL with respect to healthy retinas, that was further reduced to < 10% of the healthy values at 240 DPI (**Extended Data Fig.2**).

We next used photoreceptor-specific markers to dissect the combined effects of surgery and NP injection on photoreceptor survival at 30 and 240 DPI. Rod and cone cell bodies were individually labelled with rhodopsin or cone-arrestin antibodies, respectively, or collectively labelled with recoverin antibodies. Both rod and cone cell bodies were dramatically decreased with respect to healthy RCS-rdy retinas at 30 DPI and, even more, at 240 DPI, irrespective of whether RCS rats were non-injected or injected with either P3HT or glass NPs (**Fig.3**). In the case of recoverin staining, also labelling a subpopulation of bipolar cells (BCs), degeneration in all experimental groups of dystrophic RCS rats specifically and markedly hit the photoreceptor population, leaving BCs relatively unaffected with respect to healthy RCS-rdy rats (**Extended Data Fig.3**). We confirmed these observations by qRT-PCR analysis of retinal mRNA levels of rhodopsin and both short- and long-wave Opsin1 that are specifically transcribed by intact and viable rod and cone cell bodies. All dystrophic RCS animals, irrespective of whether they were non-implanted, implanted with P3HT-NPs or sham-implanted with glass-NPs, displayed photoreceptor-specific mRNA levels that were 2-3 orders of magnitude lower than those of age-matched non-dystrophic animals at both 30 and 240 DPI (**Extended Data Fig.4**).

The analysis of the GFAP and Iba-1 immunoreactivities, as markers of astrocyte/Muller cell gliosis and microgliosis, as well as the expression of the retinal trophic factor FGF2, revealed the presence of an inflammatory response due to degeneration in all dystrophic RCS groups at both 30 and 240 DPI, while surgery and NP microinjection were devoid of further pro-inflammatory effects (**Extended Data Fig.5**). This observation was also confirmed by the minimal (<20%) overlap of P3HT fluorescence with the astrocyte/microglial markers (**Supplementary Fig.8**). These results exclude the presence of trophic and/or proinflammatory effects triggered by the surgical procedure or the presence of NPs that might slow down photoreceptor degeneration and bias the subsequent functional rescue tests.

P3HT-NPs rescue visual responses in dystrophic RCS rats

The pupillary light reflex (PLR) is an autonomic reflex integrated at subcortical level driven by the complementary function of the rod-cone and the melanopsin-expressing RGC systems [41]. We evaluated the extent of pupillary constriction in response to light beams of various intensities (1-20 lux) as an index of light sensitivity (**Fig.4a**) [20]. The PLR was markedly depressed in RCS rats at 4 and 11 months of age, as compared to healthy age-matched RCS-rdy controls at all irradiation intensities (**Fig.4b,c**). In contrast, P3HT-NP-injected RCS rats displayed a clear-cut increase in the evoked pupil constriction over the whole range of irradiances at both 30 and 240 DPI with respect to either untreated or sham-injected RCS animals (**Fig.4b,c**;**Supplementary Movies S1,S2**). Notably, the PLR responses of P3HT-NP-injected RCS rats fully matched those of healthy controls at both 30 and 240 DPI, indicating a persistent *restitutio ad integrum*. Interestingly, the area under the PLR dose-response curve revealed that, while PLR performances tended to naturally decrease with age, they remained stable over time in RCS animals that received P3HT-NPs (**Fig.4d**).

We next assessed the electrophysiological restoration of normal visual functions at the cortical level. We firstly measured the amplitude of electrical responses of the V1 cortex to flashes of light using extracellular recordings of VEPs in the binocular area of V1 (**Fig.5a**) [20,42]. VEP responses in untreated dystrophic RCS rats were markedly impaired with respect to healthy RCS-rdy controls already at 4 and even more at 11 months of age, becoming closer to the noise band (**Fig.5c,e**), in agreement with data on light sensitivity and spatial acuity reported for the RCS rat strain [43]. A substantial rescue of light sensitivity was observed in RCS rats injected with P3HT-NPs at 30 DPI, with amplitudes of the V1 signal approaching the response of healthy RCS-rdy controls (**Fig.5c**;**Supplementary Fig.9a**). The rescue of VEP responses in P3HT-NP injected RCS rats after 240 DPI were qualitatively and quantitatively similar to those observed at 30 DPI, indicating the persistence of the effects over time after a single microinjection (**Fig.5e**;**Supplementary Fig.9b**).

We next evaluated the quality of the recovered sight by examining the spatial resolution (i.e., visual acuity) in response to patterned visual stimuli of increasing spatial frequency (**Fig.5b**) [20,42]. While untreated RCS rats displayed a marked impairment in visual acuity (**Fig.5d,f**; **Figs S10,S11**), P3HT-NP injected RCS rats displayed a full recovery of acuity to the levels of healthy RCS-rdy controls at 30 DPI (**Fig.5d;Supplementary Fig.11a**)**.** The complete rescue of spatial acuity in P3HT-NP-injected RCS rats was fully preserved also at 240 DPI (**Fig.5f;Supplementary Fig.11b**). In spite of the improvement of VEP responses by P3HT-NPs, the increased latency of dystrophic RCS rats was not significantly rescued by the treatment (**Extended Data Fig.6a**).

To clarify that the visual rescue was not due to residual or "regenerating" photoreceptors and

that P3HT-NPs are indeed responsible for the cortical responses, we measured flash-evoked VEP amplitudes in response to: (i) white light (as done above); (ii) red light, known not to stimulate photoreceptor responses in the healthy rat retina, but still able to partially stimulate P3HT-NPs; and (iii) near-infrared (NIR), which stimulates neither photoreceptor nor P3HT-NPs (**Fig.5g**). While white light evoked significant VEP responses in healthy RCS-rdy rats and P3HT-NP injected dystrophic animals and NIR light did not evoke responses in any of the four experimental groups, red light triggered a VEP response only in RCS rats bearing P3HT-NPs (**Fig.5h; Supplementary Fig.12**). Interestingly, the latencies of VEP responses to white and red light were not significantly different, confirming the same underlying mechanism (**Extended Data Fig.6b**). These data unequivocally prove that the rescue of visual cortical responses is indeed attributable to P3HT-NPs and not to surviving photoreceptors.

To obtain an independent proof of the light-evoked activation of the visual cortex by retinal signals, we evaluated the V1 metabolic activity by positron emission tomography neuroimaging of the glucose analogue ^{18}F-fluoro-deoxyglucose (^{18}F-FDG) [20]. The tracer enters neuronal cells as a function of their glucose consumption, is phosphorylated by hexokinase and accumulates in the cytosol [44], thus providing a 3D map of the metabolic activity of V1. Standardized uptake values (SUV) in the V1 region identified by MRI scans were used to estimate the extent of V1 activation in ^{18}F-FDG-injected animals subjected to a 40 min visual stimulation with light flashes (**Extended Data Fig.7a**) [45]. Untreated dystrophic RCS animals displayed a lower SUV in V1 with respect to age-matched RCS-rdy controls (**Extended Data Fig.7b**). Consistent with the recovery of visual functions assessed by *in vivo* electrophysiology, P3HT-NP injected, but not sham-injected, RCS rats showed a significant increase in average SUV at 240 DPI and became indistinguishable from non-injected RCS-rdy controls.

We finally tested whether bilaterally injected P3HT-NPs could rescue visually driven behavioural activity in dystrophic RCS animals using the light-dark box test and evaluating the latency of escape from the illuminated area (5-lux) and the percentage of time spent in the dark (**Fig.6a**) [20,46]. Untreated RCS rats at both 4 and 11 months of age displayed a significantly longer latency of escape and no preference for the dark compartment with respect to age-matched RCS-rdy controls (**Fig.6b-e**). Strikingly, P3HT-NP-injected, but not sham-injected, RCS rats showed a full recovery in both latency of escape and preference for the dark compartment to the levels of RCS-rdy controls at both 30 and 240 DPI (**Fig.6b-e**;**Supplementary Movies S3,S4**), in the absence of any change in the overall motor activity (**Supplementary Fig.13**).

The above data indicate that the visual rescue by P3HT-NPs is not attributable to trophic or pro-inflammatory effects. To confirm that, a subpopulation of rats belonging to the four experimental groups that underwent all individual tests (a total of 21 rats at 30 DPI and 16 at 240 DPI) was subjected to a correlative analysis of the principal morpho-functional retinal components, in which functional performances at 30 and 240 DPI were individually correlated with either photoreceptor

survival (**Supplementary Fig.14**) or inflammatory/trophic biomarkers (**Supplementary Fig.15**). To better understand the effects of the P3HT-NP injection, we first mapped the cross-correlation between these variables and observed a significant co-linearity among many of them (**Extended Data Fig.8**). Except for P3HT-NP injected RCS rats, photoreceptor cell counts were strongly correlated with visual acuity and visually driven behavioural responses and inversely correlated with inflammatory markers. We then decided to decompose all values in 3 integrated variables indicating visual responses, inflammatory response, and residual photoreceptor counts (**Extended Data Fig.9**). In both time windows, data clusters were well separated, with healthy RCS-rdy rats showing the highest visual responses and photoreceptor counts, and the lowest score for inflammatory markers. Both sham-injected and P3HT-NP injected RCS rats showed no recovery in the photoreceptor cell body numbers ($p>0.45$) or any worsening of the inflammatory state ($p>0.55$) with respect to untreated RCS rats. Despite the photoreceptor depletion and inflammatory state, P3HT-NP injected RCS rats show unequivocally and significantly stronger visual responses than the untreated or sham-injected controls, fully supporting a direct role of P3HT-NPs in visual rescue and ruling out the contribution of trophic effects. No significant correlation of visual performances with the NP layer thickness or the NP/ONL volume ratio were observed, also given the highly reproducible distribution of NPs in the outer retina (**Supplementary Fig.16**).

Conjugated polymer nanoparticles as a liquid retinal prosthesis

Organic semiconductors are carbon-based materials similar to most natural pigments. Among them, conjugated polymers have electron delocalization along their backbone. This bestows optoelectronic properties typical of semiconductors, while preserving mechanical and processing properties typical of plastic. Akin to biological molecules, conjugated polymers are ideal for interacting with biological tissues, being highly biocompatible, soft and conformable and non-inflammatory [12,13]. Here, we propose a new "*liquid retina device*" made of an aqueous suspension of single component polymeric NPs in the absence of a hole-acceptor layer. Sterile and surfactant-free sub-μm P3HT-NPs, obtained by the re-precipitation method in which nucleation of NPs is triggered by the rapid change in solvent polarity favouring π–π stacking and hydrophobic interactions, are effective bio-actuators characterized by high surface/volume ratio, large optical absorption cross-section, effective heat dissipation, high biocompatibility due to the intrinsic affinity of their carbon-based chemical structure with that of biomolecules and high potential for spatial resolution, with neighbour distances in the range of foveal cones [47].

A recent work [32] shows that water polarization at the polymer surface induces a downshift of the frontier orbital energy, mimicking semiconductor band bending. Upon photoexcitation, negative charge accumulates at the surface separating from positive charge in the bulk, with oxygen doping reinforcing this effect. Light-evoked depolarization and neurons firing by P3HT-

NPs has a capacitive origin and is made possible by the light-dependent charging of the NP surface coupled to a loose-patch conformation of the junctional surface in which the neuronal membrane closely wraps the NPs generating a virtual cleft of less than 20 nm and a GΩ seal with the extracellular medium. With cleft resistances above 10-100 MΩ, mV depolarizations occur at physiological light intensities. Although the effect has the same size of a postsynaptic potential in central synapses, extensive temporal and spatial summation can occur to reach the firing threshold of the neuron.

These unique features became even more substantial when P3HT-NPs are microinjected, with the minimally invasive procedure, in the subretinal space of blind rats where they fully rescue subcortical, visual responses, visual acuity and metabolic activation of the V1 cortex and light-driven behaviours to the levels of the healthy controls. The retinal responses evoked by P3HT-NP photo-stimulation in degenerate retinas are characterized by a longer latency than those of healthy retinas, likely due to the extensive rewiring of degenerate retinas [20,30] and to the temporal/spatial summation of photo-potentials needed to trigger RGC firing. Notably, P3HT-NPs evenly distributed throughout the subretinal space after injection, did not show any tendency to migrate toward the inner retinal layers and maintained the original subretinal distribution over time up to 8 months after injection, ruling out a wide-body diffusion of the injected NPs or clearance by neurons, astrocytes or microglia.

The visual rescue obtained with P3HT-NPs is not due to an increased survival of residual photoreceptors, but to a direct effect of the polymeric interface. In fact: (i) NP-injected pink-eyed RCS rats display an extremely severe photoreceptor degeneration with a dramatic depletion of the retinal mRNAs for rhodopsin and cone opsins and no signs of photoreceptor regeneration following surgery in NP injection; (ii) sham-operated RCS rats do not experience any detectable improvement in visual function and their performance fully overlaps with that of untreated RCS rats; (iii) visual stimulation with red light, to which healthy rat photoreceptors are blind, elicits visual cortical signals only in RCS rats injected with P3HT-NPs.

Conclusions

Several NPs have been recently proposed for neuronal photostimulation or for ameliorating degenerative blindness. Rare earth NPs are effective in preventing or slowing-down photoreceptor degeneration induced by excessive free radical production [49]. Neuron-targeted gold NPs can trigger photo-thermal neuronal stimulation [50]. Infrared-sensitive upconverting NPs exciting optogenetic actuators [26] endow retina with infrared sensitivity [27]. In this scenario, the conjugated polymer NPs reported in this study represent the first attempt to rescue sensitivity and spatial discrimination in degenerate retinas in response to visible light. Although the limited visual acuity of the animal model does not allow to conclusively demonstrate the spatial resolution potential of P3HT-NPs, the grating acuity obtained in the dystrophic RCS rat

equals the best that can be achieved by current implants. The simpler surgical operation with respect to the implantation of a retinal prosthesis and the wide retinal coverage, potentially restoring the complete visual field, opens a new avenue in the clinical applications of CPs in degenerative blindness. The potential for high spatial resolution of P3HT-NPs may extend their applicability to earlier stages of RP and atrophic AMD, once their efficacy will be demonstrated in high-resolution retinas. Working as non-genetic light actuators for neuronal activation, semiconducting polymer NPs have a high potential for biomedical applications in degenerative retinal diseases and, possibly, in central nervous system diseases.

References

1. Pascolini, D. & Mariotti, S.P. Global estimates of visual impairment: 2010. *Br. J. Ophthalmol.* **9**, 614-618 (2012).

2. Provis, J.M., Penfold, P.L., Cornish, E.E., Sandercoe, T.M. & Madigan, M.C. Anatomy and development of the macula: specialization and the vulnerability to macular degeneration. *Clin. Exp. Optom.* **88**, 269-281 (2005).

3. Ziccardi, L. *et al.* Gene therapy in retinal dystrophies. *Int. J. Mol. Sci.* **20**, 22 (2019).

4. Maeda, A., Mandai, M. & Takahashi, M. Gene and induced pluripotent stem cell therapy for retinal diseases. *Annu. Rev. Genom. Hum. Genet.* **20**, 201-216 (2019).

5. Simunovic, M.P. *et al.* Optogenetic approaches to vision restoration. *Exp. Eye Res.* **178**, 15-26 (2019).

6. Scholl, H.P. *et al.* Emerging therapies for inherited retinal degeneration. *Sci. Transl. Med.* **8**, 368rv6 (2016).

7. Benfenati, F. & Lanzani, G. New technologies for developing second generation retinal prostheses. *Lab Anim (NY)* **47**, 71-75 (2018).

8. Bloch, E., Luo, Y. & da Cruz, L. Advances in retinal prosthesis systems. *Ther. Adv. Ophthalmol.* **11**, 2515841418817501 (2019).

9. Dagnelie, G. *et al.* Argus® II Study Group. Performance of real-world functional vision tasks by blind subjects improves after implantation with the Argus® II retinal prosthesis system. *Clin. Exp. Ophthalmol.* **45**, 152-159 (2017).

10. Stingl, K. *et al.* Artificial vision with wirelessly powered subretinal electronic implant alpha-IMS. *Proc. Biol. Sci.* **280**, 20130077 (2013).

11. Lorach, H. *et al.* Photovoltaic restoration of sight with high visual acuity. *Nat. Med.* **21**, 476-482 (2015).

12. Manfredi, G., Colombo, E., Barsotti, J., Benfenati, F. & Lanzani, G. Photochemistry of organic retinal prostheses. *Annu. Rev. Phys. Chem.* **70**, 99-121 (2019).

13. Rivnay, J., Wang, H., Fenno, L., Deisseroth, K. & Malliaras, G.G. Next-generation probes, particles, and proteins for neural interfacing. *Sci. Adv.* **3**, e1601649 (2017).

14. Ghezzi, D. *et al.* A hybrid bioorganic interface for neuronal photoactivation. *Nat. Commun.* **2**, 166 (2011).

15. Feyen, P. *et al.* Light-evoked hyperpolarization and silencing of neurons by conjugated polymers. *Sci. Rep.* **6**, 22718 (2016).

16. Ghezzi, D. *et al.* A polymer optoelectronic interface restores light sensitivity in blind rat retinas. *Nat. Phot.* **7**, 400-406 (2013).

17. Gautam, V., Rand, D., Hanein, Y. & Narayan, K.S. A polymer optoelectronic interface provides visual cues to a blind retina. *Adv. Mater.* **26**, 1751-1756 (2014).

18. Gal, A. *et al.* Mutations in MERTK, the human orthologue of the RCS rat retinal dystrophy gene, cause retinitis pigmentosa. *Nat. Genet.* **26**, 270-271 (2000).

19. Antognazza, M.R. *et al.* Characterization of a polymer-based fully organic prosthesis for implantation into the subretinal space of the rat. *Adv. Healthc. Mater.* **5**, 2271-2282 (2016).

20. Maya-Vetencourt, J.F. *et al.* A fully organic retinal prosthesis restores vision in a rat model of degenerative blindness. *Nat. Mater.* **16**, 681-689 (2017).

21. Di Maria, F., Lodola, F., Zucchetti, E., Benfenati, F. & Lanzani, G. The evolution of artificial light actuators in living systems: from planar to nanostructured interfaces. *Chem. Soc. Rev.* **47**, 4757-4780 (2018).

22. Tian, B. *et al.* Roadmap on semiconductor-cell biointerfaces. *Phys. Biol.* **15**, 031002 (2018).

23. Rossi, E.A. & Roorda, A. The relationship between visual resolution and cone spacing in the human fovea. *Nat. Neurosci.* **13**, 156-157 (2010).

24. Feng, L. *et al.* Conjugated polymer nanoparticles: preparation, properties, functionalization and biological applications. *Chem. Soc. Rev.* **42**, 6620-6633 (2013).

25. Colombo, E., Feyen, P., Antognazza, M.R., Lanzani, G. & Benfenati, F. Nanoparticles: a challenging vehicle for neural stimulation. *Front. Neurosci.* **10**, 105 (2016).

26. Chen, S. *et al.*, Near-infrared deep brain stimulation via upconversion nanoparticle-mediated optogenetics. *Science* **359**, 679-684 (2018).

27. Ma, Y. *et al.* Mammalian near-infrared image vision through injectable and self-powered retinal nanoantennae. *Cell* **177**, 243-255.e15 (2019).

28. Tuncel, D. & Demir, H.V. Conjugated polymer nanoparticles. *Nanoscale* **2**, 484-494 (2010).

29. Zangoli, M. *et al.* Engineering thiophene-based nanoparticles to induce phototransduction in live cells under illumination. *Nanoscale* **9**, 9202-9209 (2017).

30. Pu, M., Xu, L. & Zhang, H. Visual response properties of retinal ganglion cells in the Royal College of Surgeons dystrophic rat. *Invest. Ophthalmol. Vis. Sci.* **47**, 3579-3585 (2006).

31. Martino, N. *et al.* Photothermal cellular stimulation in functional bio-polymer interfaces. *Sci. Rep.* **5**, 8911 (2015).

32. Mosconi, E. *et al.* Surface polarization drives photo-induced charge separation at the P3HT/water interface. *ACS Energy Lett.* **1**, 454-463 (2016).

33. Fendyur, A., Mazurski, N., Shappir, J. & Spira, M.E. Formation of essential ultrastructural interface between cultured hippocampal cells and gold mushroom-shaped MEA - toward "IN-CELL" recordings from vertebrate neurons. *Front. Neuroeng.* **4**, 14 (2011).

34. Shmoel, N. *et al.* Multisite electrophysiological recordings by self-assembled loose-patch-like junctions between cultured hippocampal neurons and mushroom-shaped microelectrodes. *Sci. Rep.* **6**, 27110 (2016).

35. Hanson, L., Lin, Z.C., Xie, C., Cui, Y. & Cui, B. Characterization of the cell-nanopillar interface by transmission electron microscopy. *Nano Lett.* **12**, 5815-5820 (2012).

36. Pardue, M.T. *et al.* Neuroprotective effect of subretinal implants in the RCS rat. *Invest. Ophthalmol. Vis. Sci.* **46**, 674-682 (2005).

37. Morimoto, T. *et al.* Transcorneal electrical stimulation promotes the survival of photoreceptors and preserves retinal function in Royal College of Surgeons rats. *Invest. Ophthalmol. Vis. Sci.* **48**, 4725-4732 (2007).

38. Zhou, W.T. *et al.* Electrical stimulation ameliorates light-induced photoreceptor degeneration *in vitro* via suppressing the proinflammatory effect of microglia and enhancing the neurotrophic potential of Müller cells. *Exp. Neurol.* **238**, 192-208 (2012).

39. Lorach, H. *et al.* Long-term rescue of photoreceptors in a rodent model of Retinitis pigmentosa associated with MERTK mutation. *Sci. Rep.* **8**, 11312 (2018).

40. LaVail, M.M. & Battelle, B.A. Influence of eye pigmentation and light deprivation on inherited retinal dystrophy in the rat. *Exp. Eye Res.* **21**, 167-192 (1975).

41. Lucas, R.J. *et al.* Diminished pupillary light reflex at high irradiances in melanopsin-knockout mice. *Science* **299**, 245-247 (2003).

42. Maya Vetencourt, J.F. *et al.* The antidepressant fluoxetine restores plasticity in the adult visual cortex. *Science* **320**, 385-388 (2008).

43. McGill, T.J., Douglas, R.M., Lund, R.D. & Prusky, G.T. Quantification of spatial vision in the Royal College of Surgeons rat. *Invest. Ophthalmol. Vis. Sci.* **45**, 932-936 (2004).

44. Phelps, M.E. Positron computed tomography studies of cerebral glucose metabolism in man: theory and application in nuclear medicine. *Semin. Nucl. Med*. **11**, 32-49 (1981).

45. Hustinx, R., Smith, R.J., Benard, F., Bhatnagar, A. & Alavi, A. Can the standardized uptake value characterize primary brain tumors on FDG-PET? *Eur. J. Nucl. Med.* **26**, 1501-1509 (1999).

46. Bourin, M. & Hascoet, M. The mouse light/dark box test. *Eur. J. Pharmacol.* **463**, 55-65 (2003).

47. Smith, G. & Atchinson, D.A. The Eye. In: *The Eye and Visual Optical Instruments*, pp 291-316. Cambridge University Press (1997).

48. Shapiro, M.G., Homma, K., Villarreal, S., Richter, C.P. & Bezanilla, F. Infrared light excites cells by changing their electrical capacitance. *Nat. Commun.* **3**, 736 (2012).

49. Chen, J., Patil, S., Seal, S. & McGinnis, J.F. Rare earth nanoparticles prevent retinal degeneration induced by intracellular peroxides. *Nat. Nanotechnol.* **1**, 142-150 (2006).

50. Carvalho-de-Souza, J.L. *et al.* Photosensitivity of neurons enabled by cell-targeted gold nanoparticles. *Neuron* **86**, 207-217 (2015).

Acknowledgements

The Authors thank dr. M.M. La Vail (Beckman Vision Centre, University of California San Francisco, CA) for kindly providing non-dystrophic RCS-rdy+ and dystrophic RCS rats; drs. N. De Petrocellis and N. Forte (CNR Institute for Biomolecular Chemistry, Pozzuoli, Italy) for hTRPV1 stably transfected HEK293 clones, dr. E. Lingueglia (CNRS Institute of Molecular and Cellular Pharmacology, Valbonne, France) for kindly providing the cDNA for ASIC1a channel, drs. A. Desii, S. Francia and M. Salerno (Istituto Italiano di Tecnologia, Genova, Italy) for help in the preparation and characterization of NPs, M. Cilli and A. Buschiazzo (IRCCS Ospedale Policlinico San Martino, Genova, Italy) for assistance in the surgical procedures and help in PET imaging, R. Ciancio, I. Dall'Orto, A. Mehilli, R. Navone and D. Moruzzo (Istituto Italiano di Tecnologia, Genova, Italy) for technical assistance. The work was supported by the Italian Ministry of Health (project RF-2013-02358313 to GP, GL and FB), Fondazione Cariplo (project 2018-0505 to GL, FB and GP), Compagnia di San Paolo (project 9798 to JFMV), H2020-MSCA-ITN 2019 “Entrain Vision” (project 861423 to F.B.) and EuroNanoMed3 (project 2019-132 "NanoLight" to FB). The support of the Ra.Mo. Foundation (Milano, Italy), Rare Partners srl (Milano, Italy) and Fondazione 13 Marzo (Parma, Italy) is also acknowledged.

Author contributions

J.F.M.V. followed all *in vivo* experiments by performing electrophysiology and behavioural analyses under the supervision of F.B. and assisted in the OCT and PET trials; G.P., M.M. and A.Ru. developed and executed the subretinal microinjection; M.M. performed OCT analysis; G.M., J.B. and F.D.M. fabricated the NPs and characterized them under the supervision of G.L.; E.C., S.D.M., M.D.F., E.D.P., M.D. M.B. performed the *in vitro*/*ex vivo* electrophysiological and EM experiments on HEK cells, neurons and retinal explants under the supervision of F.B.; V.C., F.T., L.E., D.S., C.M. executed PET experiments under the supervision of G.S.; D.S., G.M. and

C.E. performed histological analyses under the supervision of S.D.M. and J.F.M.V.; A.Ro. performed the qRT-PCR experiments; J.F.M.V., G.L., and F.B. wrote the manuscript; F.P. revised the manuscript; F.B., G.P., J.F.M.V. and G.L., conceived, supervised, and financed the project. All authors discussed the experimental results and commented on the manuscript.

Data availability statement

The data that support the plots within this paper together with other findings of this study are available from the corresponding author upon reasonable request.

Competing interests

The P3HT-NPs studied in this paper are the subject of the US patent application US 16/005,248 "Eye-injectable polymeric nanoparticles and method of use therefor" by Istituto Italiano di Tecnologia and Ospedale Sacrocuore Don Calabria, with J.F.M.V., M.M., G.P., F.B. and G.L. as inventors. The other authors declare no competing financial interests.

Additional Information

Supplementary information is available in the online version of the paper. Reprints and permission information is available online at www.nature.com/reprints. Correspondence and requests for materials should be addressed to FB and GL.

Legends to the Main Figures

Figure 1. P3HT-nanoparticles form a tight seal with the neuronal membrane and trigger light-evoked neuronal stimulation through a capacitive mechanism. (a) SEM images of P3HT-NPs generated with the reprecipitation method and of control Glass-NPs of similar size. P3HT-NPs sized by differential centrifugation and DLS as shown in Figure S2. **(b)** *Top:* Lateral projection of confocal z-stack fluorescence images of calcein-labelled primary neurons layered on coverslips drop-casted with P3HT-NPs. NPs (intrinsic red fluorescence) are visibly engulfed by the neuronal cell bodies and processes. *Bottom:* Ultrastructural analysis of neuron-NP interactions before and after sectioning of standard SEM preparations *(left*) and of resin-embedded FIB cross-sections (*right*). The results are representative of n=3 independent neuronal preparations. NPs establish a very tight (< 20 nm) contact with the neuronal junctional membrane, with a quasi-virtual cleft secluded from the extracellular space. **(c)** Example of a light-stimulated (green spot) patched RGC puffed with P3HT-NPs (*left).* Representative averaged current-clamp traces (mean±SD; $I_{holding}$ = 0 pA) of an RGC from the retina of 12-14 months-old RCS rats in the presence of P3HT-NPs in response to 540 nm flashes (40 mW/mm^2, 500 ms; *right*). The results are statistically analysed in panel d. **(d)** *Left:* Peristimulus time histogram of the firing activity (means±sem). *Right*: Box plots of the RGC membrane potential in the dark and after light stimulation (n=5 RCS rats; *p<0.05, Wilcoxon's one-tailed test). **(e)** Schematic representation of a retinal explant with the RGC layer facing the MEA electrodes and the subretinal NP-injection under the choroid. Green arrows represent the direction of the light stimuli *(left)*. Representative raster plots of the overall firing activity of RGCs in the presence of either P3HT-NPs or Glass-NPs (500 ms light stimulation 40 mW/mm^2 @ 540 nm; *middle*). Percent light-evoked variation in firing of the recorded RGCs with respect to the baseline normalized to the firing in the absence of NPs (Control; *right*). In the dose-response plot of the normalized firing activity, only neurons displaying a significant (two-sided Student's *t*-test) light-induced firing modulation with respect to the baseline were considered. * p<0.05, **** p<0.0001, two-way ANOVA/Fisher's LSD test. P3HT-NPs: 35, 55, 112, 224 neurons/21 retinas; Glass-NPs: 25, 38, 83, 167 neurons/18 retinas; Control: 21, 44, 91, 192/19 retinas; for 1, 7, 18, 40 mW/mm^2 stimuli, respectively. **(f)** The latency of ON responses in healthy (RCS-rdy) retinas and P3HT-mediated ON-like responses in dystrophic (RCS) retinas was measured in 12-14 months-old rats as the time needed to reach the peak firing rate with respect to the stimulus onset (n = 52 neurons/15 non-injected RCS-rdy retinas and n = 207 neurons/10 RCS-injected retinas) **** p<0.0001, two-sided Student's *t*-test. **(g)** A cartoon of a NP engulfed by the neuronal membrane with the current paths and the nanoparticle-cell membrane equivalent circuit. **(h)** *Left:* Simulated junctional and extra-junctional membrane voltage variation upon 50 ms light pulse at 40 mW/mm^2 for an interface of a single P3HT-NP of 400 nm, using the fit parameters reported in the Supplementary

Materials. The polarity of the potential change in the cleft is opposite to the extra-junctional one. *Right:* Junctional and extra-junctional membrane potential peak variation as a function of the cleft resistance plot. Data in **d**,**e** are means±sem. Box plots in **d**,**f** represent the median (centre line), mean (square), 25^{th}-75^{th} percentiles (box) and the limit of 3-fold the interquartile range. For exact p values, see **Supplementary Table 3.**

Figure 2. Subretinally microinjected P3HT-nanoparticles display wide and stable retina coverage and are not cleared over time. (a) *Left:* Transversal retinal sections from dystrophic RCS rats injected with either endogenously fluorescent P3HT-NPs or fluorescent Glass-NPs at 30 DPI. NP fluorescence (red) was merged with bisbenzimide nuclear staining (blue). *Right:* Percent frequency distribution of the volume of P3HT- (red) and Glass- (yellow) NP clusters (5 µm bins) at 30 DPI. The analysis was performed on z-stack confocal images of retinal sections (50 µm thickness) by a custom-generated macro running with ImageJ. $p>0.10$, two-sided Kolmogorov-Smirnov test. **(b)** *Left:* Full equatorial reconstruction of from dystrophic retinas from RCS rats injected with either endogenously fluorescent P3HT-NPs or fluorescent Glass-NPs at 30 DPI, showing the diffusion of NPs (red) in the whole subretinal space, with no tendency to permeate the internal retinal layers (insets at higher magnification). *Right:* Bar plots of the total NP volume in the subretinal space and the percent retinal coverage for P3HT-NPs or fluorescent Glass-NPs at 30 DPI. Individual experimental points are superimposed. $p>0.05$, two-sided Mann-Whitney's *U*-test. **(c)** *Left:* Transversal retinal sections from dystrophic RCS rats injected with P3HT-NPs at 240 DPI. *Middle:* Comparison of the percent frequency distribution of the P3HT-NP cluster volume (5 µm bins) at 30 (red) and 240 (gray) DPI. The analysis was performed as in **a**. $p>0.10$, two-sided Kolmogorov-Smirnov test. *Right:* Total P3HT-NP volume in the subretinal space at 30 and 240 DPI. Individual experimental points are superimposed. $p>0.05$, Mann-Whitney's *U*-test. Data are means ± sem of n=6 RCS rats per each experimental group (P3HT-NPs 30 DPI; Glass-NPs 30 DPI; P3HT-NPs 240 DPI). For exact p values, see **Supplementary Table 3.**

Figure 3. P3HT-nanoparticles do not promote photoreceptor survival in dystrophic retinas. Transversal sections of representative retinas were dissected at 30 DPI (**a-c**) and 240 DPI (**d-f**) from non-dystrophic controls (RCS-rdy), untreated dystrophic RCS rats (RCS) or dystrophic RCS rats injected with either P3HT-NPs (RCS+P3HT) or control Glass-NPs (RCS+Glass). Sections were immunolabelled for: the rod/cone marker recoverin (**a,d;** labelling rods, cones and on/off cone bipolar cells), rhodopsin (**b,e;** labelling rods) and cone-arrestin (**c,f;** labelling cones). Images were acquired from corresponding fields in the various retinas by taking the injection site as reference point (2 slices/retina; 3 fields/slice). The bar plots on the right (means ± sem with superimposed individual data points) report the respective photoreceptors

cell body counts. **** p<0.0001 *vs* RCS-rdy controls; Kruskal-Wallis\Dunn's tests. Sample size (experimental animals) at 30 DPI: recoverin 5, 5, 5, 5; rhodopsin 11, 9, 11, 11; cone-arrestin 5, 6, 7, 11; for RCS-rdy, RCS, RCS+P3HT and RCS+Glass, respectively. Sample size (experimental animals) at 240 DPI: recoverin 5, 5, 5, 4; rhodopsin 8, 7, 8, 8; cone-arrestin 4, 3, 4, 4; for RCS-rdy, RCS, RCS+P3HT and RCS+Glass, respectively. Dystrophic retinas display a very low density of photoreceptors that is not minimally affected by surgery- and/or NP-mediated trophic effects. In each panel, representative immunolabelled sections from non-injected healthy RCS-rdy rats and dystrophic RCS rat are shown merged with bisbenzimide staining for cell nuclei (blue). ONL, outer nuclear layer; INL, inner nuclear layer; GCL, ganglion cell layer. Scale bars, 50 μm. For exact p values, see **Supplementary Table 3.**

Figure 4. Long-term rescue of pupillary light reflex in dystrophic RCS rats injected with P3HT- nanoparticles. (a) Constriction of the pupil by light pulses as assessed using standard infrared imaging in dark-adapted RCS-rdy rats. **(b,c)** Quantification of the pupillary constriction as a function of light intensity in RCS-rdy (blue), RCS (green), RCS+P3HT-NPs (red), and RCS+Glass-NPs (yellow) rats. A full recovery of the reflex even at the lowest light intensities is observed in RCS rats injected with P3HT-NPs at both 30 (**b**) and 240 (**c**) DPI. ° 0.01<p<0.001 (30 DPI), 0.05<p<0.01 (240 DPI), RCS-rdy *vs* RCS; + 0.01<p<0.001 (30 DPI), 0.05<p<0.01 (240 DPI) P3HT-NP RCS *vs* Glass-NP RCS; repeated measures ANOVA. No differences were found between RCS-rdy and RCS injected with P3HT-NPs. **(d)** Box plots of the areas under the light dose-response curves at 30 (open boxes) and 240 (dashed boxes) DPI for the four experimental groups. While a progressive decay of pupillary responses (lines joining the median values) is observed with age in RCS-rdy, RCS and RCS injected with Glass-NPs due to progressive photoreceptor loss, RCS rats injected with P3HT-NPs fully preserved the improvement in pupillary reactivity up to 240 DPI. *** p<0.001, one-way ANOVA/Tukey's test. Data in **b**,**c** are means±sem. Box plots in **d** represent the median (centre line), mean (square), 25^{th}-75^{th} percentiles (box) and the limit of 3-fold the interquartile range. Sample size (experimental animals): RCS-rdy, n=8 and 7; RCS, n=11 and 6; RCS+P3HT-NPs, n=24 and 6; RCS+Glass-NPs, n=18 and 8, for 30 and 240 DPI, respectively. For exact p values, see **Supplementary Table 3.**

Figure 5. Long-term rescue of V1 cortical responses in response to flash and patterned illumination in dystrophic RCS rats injected with P3HT-nanoparticles. (a,b) Experimental setup for VEP recordings in V1 in response to either flash stimuli (**a**; 20 cd m^{-2}; 200 ms, 1 Hz) or to horizontal sinusoidal gratings of increasing spatial frequency (**b**; 0.1 to 1 cycle/degree of visual angle) administered at 1 Hz. (**c,e)** VEP recordings in V1 in response to flash stimuli show a significant improvement of light sensitivity in RCS rats injected with P3HT-NPs at both 30 (**c**) and

240 (**e**) DPI. **(d,f)** The electrophysiological analysis of VEP recordings in response to horizontal sinusoidal gratings reveals a full recovery of visual acuity at both 30 (**d**) and 240 (**f**) DPI. * p<0.05; ** p<0.01; *** p<0.001; NS, p>0.05; one-way ANOVA/Tukey's test. (**g,h**) To demonstrate the role of P3HT-NPs in the light-evoked VEP responses, a separate cohort of animals at 30 DPI was stimulated with white, red and near infrared (NIR) flash stimuli (20 cd m^{-2}; 200 ms, 1 Hz). The absorbance spectrum of P3HT-NPs (**g**) shows that P3HT is activated by red stimuli (although to a lesser extent compared to while light), but not by IR. The VEP amplitude evoked by white, red and IR flash stimuli in the four experimental groups (**h**) reveals that healthy RCS-rdy and dystrophic RCS rats are blind to red and NIR, and that only the P3HT-NP injected, but not the sham-injected, group displays a significant VEP response to red, but not to NIR stimuli. * p<0.05; ** p<0.01; *** p<0.001; one-way ANOVA/Tukey's test. In all VEP amplitude plots (**c,e,h**) the average 2xSD noise band has been reported over the baseline (blue area). Box plots in **c-f** represent the median (centre line), mean (square), 25^{th}-75^{th} percentiles (box) and the limit of 3-fold the interquartile range. Data in **h** are means±sem with superimposed individual experimental points. Sample size in panels **c-f** (experimental animals): RCS-rdy, n=8 and 4; RCS, n=7 and 4; RCS+P3HT-NPs, n=12 and 4; RCS+Glass-NPs, n=7 and 4, for 30 and 240 DPI, respectively. Sample size in panel **h** (experimental animals): RCS-rdy, n=8; RCS, n=4; RCS+P3HT-NPs, n=7; RCS+Glass-NPs, n=4. For exact p values, see **Supplementary Table 3.**

Figure 6. Long-term rescue of visually evoked behaviour in dystrophic RCS rats injected with P3HT-nanoparticles. The light-dark box test **(a)** revealed the reinstatement of light sensitivity in RCS rats injected with P3HT-NPs. The behavioural performance was evaluated based on the escape latency from the light compartment (**b,d**) and the overall time spent in the dark compartment (**c,e**) at both 30 (**b,c**) and 240 (**d,e**) DPI. ** p<0.01; *** p<0.001; NS, p>0.05; one-way ANOVA/Tukey's test. Box plots in **b-e** represent the median (centre line), mean (square), 25^{th}-75^{th}percentiles (box) and the limit of 3-fold the interquartile range. Sample size (experimental animals): RCS-rdy, n=12 and 7; RCS, n=10 and 9; RCS+P3HT-NPs, n=24 and 8; RCS+Glass-NPs, n=10 and 8, for 30 and 240 DPI, respectively. For exact p values, see **Supplementary Table 3.**

Online Methods

Production and characterization of P3HT-NPs. P3HT was synthesized by oxidative polymerization of 3-hexyl-thiophene (3HT; 1 g in 40 ml of $CHCl_3$) with ferric chloride according to a known procedure [51]. The method displayed high reproducibility in the characteristics of the polymer, such as regio-regularity (as estimated from ^{1}H-NMR), dispersity and spectroscopic features. The P3HT-NPs were then obtained from freshly prepared P3HT solution in common organic solvents using the re-precipitation technique in the absence of surfactants, as previously described [51,52]. Briefly, P3HT (8 mg) dissolved in 300 µl tetrahydrofuran was added dropwise via a Hamilton syringe to 4 ml of sterilized milliQ-water under magnetic stirring. The obtained suspension was subjected to dialysis (12,000 g/mol cutoff) against 2 l of sterile milliQ-water for 2 days to remove the residual organic solvent. Differential centrifugation was used to separate P3HT-NPs into fractions of different size [29]. The dispersed fraction was collected for biological use and further characterized. The whole process was carried out under sterile conditions. As a control, non-fluorescent and fluorescent glass (SiO_2) NPs of comparable size were obtained from Microparticles GmbH and Micromod Partikeltechnologie GmbH respectively (SiO_2-R-L3235, 259 nm nominal diameter, sicastar®-redF, excitation: 569 nm, emission: 585 nm, 300 nm nominal diameter) and autoclave sterilized. Glass- and P3HT-NPs were characterized by scanning electron microscopy (SEM) and dynamic light scattering (DLS). Briefly, for SEM imaging, a drop of NP solution was deposited on glass coverslip; coverslips were then sputter-coated with a 10 nm layer of gold in an Ar-filled chamber (Cressington, Sputter Coater 208HR) and imaged using a JEOL JSM-6490LA scanning electron microscope (JEOL Ltd, Tokyo, Japan). NPs were characterized by size in distilled water by DLS technique using Malvern Zetasizer NanoZS (Malvern Panalytical Ltd., Malvern, UK). Glass- and P3HT-NPs were sonicated for 1 min using a Branson 2510 bath sonicator (Branson Ultrasonic, Danbury, CT, USA). The size of NPs dispersed in deionized water was determined at a concentration of 1 mg/ml. Measurements were conducted at 25 °C by transferring 1 ml of stock solution to a square disposable cuvette for DLS analysis. A 50-mW laser at 638 nm wavelength was used as light source. For each sample, measurements were recorded at 173° (backscatter) detection angle and performed in triplicate, each counting at least 10 runs.

Patch-clamp recordings on RGCs. Dystrophic retinas were dissected from the enucleated eyes of 12 to 14 months old RCS rats. Eyes were enucleated in dim red light and kept in carbo-oxygenated Ames medium (Sigma-Aldrich). The cornea, iris, lens, and vitreous were removed but left in contact with the sclera. Each retina was sub-divided into two pieces that were transferred to the microscope stage, continuously perfused with carbo-oxygenated Ames

medium. We puffed RGCs with 1 mg/ml P3HT-NPs using borosilicate pipettes (1-2 MΩ). For further details, see Supplementary Information.

MEA recordings on retina explants. Dystrophic retinas were dissected from the enucleated eyes of 12 to 14 months old RCS rats as described above. Retinas from 12-months old congenic non-dystrophic RCS-rdy were also employed. Each retina piece of retina was placed, RGC side down after a subretinal injection on NPs, onto a 60 electrodes MEA chip using the MEA1060-inv system (Multi Channel Systems). To investigate the involvement of TRPV and ASICs channels in the mechanism of phototransduction, Ruthenium Red (10 μM; Sigma-Aldrich) and Amiloride (100 μM; Tocris) were respectively added to the recording medium. Light-evoked extracellular activity in MEA experiments was obtained with a fibre-coupled Lumencor LED system (Spectra X) peaking at 530 nm fed to an inverted Nikon Eclipse Ti microscope. The illumination spot covered an area of about 1 mm^2 with a power density ranging from 1 to 40 mW/mm^2. Data were acquired at 25 kHz and filtered between 200 Hz and 3 kHz. Spike detection and sorting were performed using MC Rack software (Multi Channel Systems). Light-evoked firing activity was assessed by selecting those RGCs displaying a statistically significant modulation of firing that was time-locked to the light stimulus with respect to the baseline (spontaneous activity). The response latency was defined as the time needed to reach the peak firing rate starting from the onset of the light stimulus.

Cell fixation and SEM/FIB imaging. Primary cortical neurons, grown onto glass coverslips drop-casted with P3HT-NPs, were fixed at 14 DIV with a 2.5% solution of glutaraldehyde in sodium cacodylate buffer (0.1 M) for 60 min at RT. A staining in glycine 20 mM in buffer solution was performed to reduce the signal-to-noise ratio for subsequent imaging. The, a RO–T–O staining protocol was performed, followed by 1 h negative staining with 5% uranyl acetate in aqueous solution in darkness at 4 °C. A final staining of the cytoskeleton was performed in tannic acid (3 min) before embedding the samples in a thin layer of Epon resin [53]. The excess resin was removed by washing the samples in ethanol before overnight polymerization at 65 °C. After polymerization, a thin gold layer (8 nm) was deposited on the samples by plasma sputtering. Cross-sectional imaging of the fixed neurons was obtained with a dual beam Helios Nanolab 650 (ThermoFisher), which provides an electron beam (SEM), an ion beam (FIB) and a gas injection system. After coating the neuron with a thin (~0.5 μm) platinum layer via the gas injection system (GIS), the neuron was cut with the FIB with an ionic current of 9.3 nA to reveal the cell-NP interface. Finally, a polishing ionic current of 0.79 nA was exploited to allow a clear imaging of the cell interior. The ion acceleration voltage was 30 kV for all FIB processes. The neuron-NP interface was imaged by SEM at a 52° tilt angle (3 kV, 0.20 - 0.40 nA). Backscattered electrons

were collected through a TLD detector in immersion mode for improved resolution. The colours of the SEM images have been inverted to highlight the cellular components.

Retina immunohistochemistry. Experimental animals were euthanized by CO_2 inhalation followed by cervical dislocation. Eyes were enucleated keeping track of the eye orientation during the staining process. Eyes were fixed in 4% paraformaldehyde in 0.1 M phosphate-buffered saline (PBS) for six hours, extensively washed in 0.1 M PBS, and cryoprotected by equilibration with 30% sucrose. Eyecups were obtained by removing the cornea, the iris, and the lens and then embedded in OCT mounting medium (Tissue-Tek; Qiagen), frozen overnight at -20 °C and cryo-sectioned at 50 µm using an MC5050 cryostat (Histo-Line Laboratories). Sections were mounted on gelatin-coated glass slides and maintained at -20 °C until processed. We evaluated the size and the distribution of P3HT-NPs from bisbenzimide stained sections (1:300; Hoechst for 1 min at room temperature) by acquiring the endogenous P3HT fluorescence (λ_{ex}, 514 nm; λ_{em}, 600-650 nm) with a Leica SP8 confocal microscope (Leica, Wetzlar, Germany). For all the morphological analysis, we used the following protocol: sections were first incubated with 10% fetal bovine serum (FBS, Gibco) at room temperature for 1 hr to block non-specific antibody binding and then incubated overnight at 4 °C with the primary antibody of interest or with Alexa Fluor™ 488 conjugate isolectin GS-IB4 from *Griffonia simplicifolia* (1:10000; Invitrogen) at the concentrations reported in **Table 1**. Alexa Fluor 488 or 637 conjugated secondary antibodies were diluted 1:300 and incubated at room temperature for 4 hr. Retinal sections were imaged with a Leica SP8 confocal microscope (Wetzlar, Germany).

Primary Antibody	Supplier	Species	Type	Dilution
Anti-rhodopsin	Invitrogen	Mouse	Monoclonal	1:100
Anti-cone arrestin	Merck Millipore	Rabbit	Polyclonal	1:250
Anti-recoverin	Merck Millipore	Rabbit	Polyclonal	1:1000
Anti-GFAP	Sigma Aldrich	Mouse	Monoclonal	1:200
Anti-iba1	Thermo Fischer	Goat	Polyclonal	1:500
Anti-FGF2	Merck Millipore	Mouse	Monoclonal	1:150

Table 1. Primary antibody dilutions for the immunolabeling of retinal sections

Morphometric analysis of the retina. Morphometric analysis was performed on 4-12 animals per experimental group by imaging and analysing 2 slices per retina and 3 fields per slice. Acquisition parameters were kept constant throughout the imaging session for comparison purposes.

Analysis of the NP distribution. The cluster volumes and centroids of P3HT/glass NPs were evaluated in 456x456x50 μm^3 using ImageJ with an XY resolution of 2048x2048 pixels and Z steps of about 6 µm (3D Object Counter Plugin), then imported into Matlab (Mathworks) for density, distribution and centre-to-centre calculations using custom-written scripts. Cluster

density was estimated in each z-stack volume by calculating centroid centre-to-centre distance between each cluster by using the following equation:

Where D_{ij} represents the distance between two clusters i and j, x/y/z represent the Cartesian coordinates for each cluster, and r represents the average radius of each cluster. This was repeated for the number of pairs (P) of clusters for N clusters in each z-stack:

The minimum distance between each neighbouring cluster D_{ij} was averaged for each number of retinas (N), using the following equation:

before averaging all values over each condition for statistical analysis. For further details, see Supplementary Information.

Pupillary Light Reflex. Following dark adaptation for at least 1 h and a light isoflurane anaesthesia, rats were positioned with the eye to be recorded perpendicular to an infrared sensitive camera fitted with Leica macro lens. Animals were subjected to a 2 s dim green light exposure of increasing irradiance provided by an LED source (515 nm) through the same optical path administered at 10 min intervals. Sequential images were captured with a Hamamatsu camera at a 5 Hz frame rate. Background illumination was provided by an infrared LED source (850 nm) throughout the experiment. Pupil area was determined off-line from individual video frames before and after light exposure. To facilitate comparisons, pupil areas (a_i) were expressed relative to the dilated area immediately prior to each exposure (a_0). The effective intensity of each exposure was measured with a lux meter.

***In vivo* electrophysiology.** Animals were anesthetized with isofluorane (3% induction; 2% maintenance in oxygen) and placed in a stereotaxic frame. Anaesthesia level was stable throughout the experiment and ECG and body temperature (37 °C) were continuously monitored. A hole was drilled in the skull, corresponding to the binocular portion of the primary visual cortex (Oc1B). After exposure of the brain surface, the *dura mater* was gently removed, and a micropipette (2 MΩ) filled with NaCl (3 M) was inserted into the cortex 5 mm from λ (intersection between the sagittal and the lambdoid sutures). Both eyes were fixed, kept wet and open along the analysis by means of adjustable metal rings. Light sensitivity and visual acuity were measured using visual evoked potentials (VEPs) [20,42,57,58]. During recording through one eye, the other was covered by a black adhesive tape. To prevent sampling bias, VEPs were recorded at three

distinct penetrations within Oc1b, at 100 and 400 µm depths for each penetration. Signals (average of 50 sweeps) were amplified, band-pass-filtered (0.1–100 Hz), and analysed, as described previously [59]. In the case of light sensitivity, visual stimuli were flashes of the same luminance (20 cd m^{-2}; 200 ms; 1 Hz; Figure 5a) of white light (400-700 nm), red light (575-700 nm) or infrared light (750-800 nm). In the case of spatial acuity, visual stimuli were horizontal sinusoidal contrast-reversing gratings of increasing spatial frequencies (0.1 to 1 cycle/degree of visual angle) at 1 Hz (Figure 5b). All visual stimuli were generated by a VSG2/2 card running custom software, displayed on a monitor (20 x 22 cm area; 100% of contrast) positioned 20 cm from the rat's eyes and centred on the previously determined receptive fields. While light sensitivity to the various wavelengths was evaluated based on the amplitude of the VEP response to light flashes, visual acuity was obtained using white light by extrapolation to zero amplitude of the linear regression through the last 4-5 data points of VEP amplitude *versus* the log of spatial frequency [57-59]. To rule out equipment-related electrical artefacts, at the end of each session, a "control" electrophysiological recording was performed covering the animal's eyes with black adhesive. As for detection of VEPs, a deflection of the basal electrical signal in Oc1b was considered significant when it was higher than 2-fold the standard deviation of the noise [60,61]. Care was taken that the recorded signals were at comparable eccentricities in the various experimental groups. Using a homemade software (1ChVEPs), the following parameters were computed: (i) the amplitude of the signal, taken as the peak-to-baseline distance; and (ii) the latency of the signal, computed as the distance between the initiation of the light stimulus and the signal peak.

Light-dark box test. The light-dark test, based on the innate aversion of nocturnal rodents to brightly illuminated areas [20,46], was used as an index of light sensitivity. The trials were performed in a two-compartment box consisting of a "light" compartment and a "dark" compartment communicating through a small door located in a dark experimental room. After a dark adaptation for 30 min, the animal is introduced into the "light" compartment that is illuminated with a 5-lux intensity. Six-minute video recordings were performed to monitor the latency of escape from the illuminated area and the percentage of time spent in each compartment. The number of transitions between the two compartments was also monitored as an index of light-independent motor activity.

Statistics and Reproducibility. Data are expressed as box plots or means ± sem (in case of normal distribution) with n as the number of independent animals (n) or independent preparations in *in vitro*/*ex vivo* studies (n). Estimates of effects sizes were obtained by using the following formula:

$n = Z^2 \times \sigma^2 / \Delta^2$

where Z is the value of the distribution function f(α,β) (with α and β type-I and type-II errors, respectively), σ is the standard deviation of the groups and Δ the minimum percent difference thought to be biologically relevant [64] and setting Z=1.96 (based on α = 0.05 and 1-β=0.9), Δ = 0.2 (20%) and σ=0.2-03 based on similar experiments and our preliminary data. The box plots elements are the following: centre line, median (Q2); square symbol, mean; box limits, 25th (Q1)-75th (Q3) percentiles; whisker length is determined by the outermost data points within 3-fold the interquartile range (Q3-Q1). Normal distribution was assessed using D'Agostino-Pearson's normality test. To compare two sample groups, either the Student's *t*-test or the Mann-Whitney *U*-test was used. To compare more than two normally distributed sample groups, one- or two-way ANOVA followed by the Tukey's, Newman-Keuls or Fisher's LSD multiple comparison test was used. $p<0.05$ was considered significant. Statistical analysis was carried out using OriginPro-9 (OriginLab Corp.) and Prism (GraphPad Software, Inc.). The component analysis was performed using Python3 and Scikit-learn package [65]. Correlation maps were plotted using the Python3 seaborne package (http://doi.org/10.5281/zenodo.1313201). The 3 summarizing variables used for 3D analysis were obtained by normalization of the starting variables to the average of the healthy RCS-rdy group and pooling under the following three components: Visual Response = PLR + VEPs + Acuity + dark persistence; Inflammatory state = GFAP + IBA1 + FGF2; Surviving Photoreceptors: Rhodamine + cone arrestin + ONL density. The equality hypothesis among groups was conducted using a permutation test with 5% alpha-level [66]. Cluster analysis on data was conducted using a Gaussian mixture with diagonal covariance matrixes and data were plotted in a three-dimensional space using Python 3 matplotlib library [67]. For further details, see Supplementary Information.

For further details on **Fabrication of planar P3HT/PET devices**, **Studies in HEK293 cells**, **Ethical approval and animal handling, Studies in primary neurons, Surgical injection procedures, In vivo imaging of the retinal implant, RNA Preparation and real-time PCR Analysis, Positron emission tomography (PET) imaging**, see Supplementary Information.

Additional Online References

51. Barbarella, G., Bongini, A. & Zambianchi, M. Regiochemistry and conformation of poly(3-hexylthiophene) via the synthesis and the spectroscopic characterization of the model configurational triads. *Macromolecules* **27**, 3039-3045 (1994).

52. Shimizu, H., Yamada, M., Wada, R. & Okabe, M. Preparation and characterization of water self-dispersible poly(3- hexylthiophene) particles. *Polym. J.* **40**, 33-36 (2007).

53. Santoro, F. *et al.* Revealing the cell-material interface with nanometer resolution by focused ion beam/scanning electron microscopy. *ACS Nano* **11**, 8320-8328 (2017).

54. Milam, A.H., Dacey, D.M. & Dizhoor, A.M. Recoverin immunoreactivity in mammalian cone bipolar cells. *Vis. Neurosci.* **10**, 1-12 (1993).
55. Günhan, E., Van der List, D. & Chalupa L.M. Ectopic photoreceptors and cone bipolar cells in the developing and mature retina. *J. Neurosci*. **23**, 1383-1389 (2003).
56. Vandesompele, J. *et al.* Accurate normalization of real-time quantitative RT-PCR data by geometric averaging of multiple internal control genes. *Genome Biol.* **3**, RESEARCH0034 (2002).
57. Pizzorusso, T. *et al.* Structural and functional recovery from early monocular deprivation in adult rats. *Proc. Natl. Acad. Sci. U.S.A.* **103**, 8517-8522 (2006).
58. Maya-Vetencourt, J.F. *et al.* Experience-dependent expression of NPAS4 regulates plasticity in adult visual cortex. *J. Physiol.* **590**, 4777-4787 (2012).
59. Huang, Z.J. *et al.* BDNF regulates the maturation of inhibition and the critical period of plasticity in mouse visual cortex. *Cell* **98**, 739-755 (1999).
60. Porciatti, V., Pizzorusso, T. & Maffei, L. The visual physiology of the wild type mouse determined with pattern VEPs. *Vis. Res.* **39**, 3071-3081 (1999).
61. Porciatti, V., Pizzorusso, T. & Maffei, L. Electrophysiology of the postreceptoral visual pathway in mice. *Doc. Ophthal.* **104**, 69-82 (2002).
62. Paxinos, G. & Watson, C. *The rat brain in stereotaxic coordinates.* Vol. 6. Elsevier Inc. (2007).
63. Marini, C. *et al.* Direct inhibition of hexokinase activity by metformin at least partially impairs glucose metabolism and tumour growth in experimental breast cancer. *Cell Cycle* **12**, 3490-3499 (2013).
64. Krzywinski, M. & Altman, N. Power and sample size. *Nat. Meth.* **10**, 1139-1140 (2013).
65. Pedregosa, F. *et al*. Scikit-learn: machine learning in Python. *J. Mach. Learn. Res.* **12**, 2825-2830 (2011).
66. Pitman, E.J.G. Significance tests which may be applied to samples from any populations. *J. Royal Stat. Soc.* 4 (Suppl.), 119 (1937).
67. Hunter, J.D. Matplotlib: a 2D graphics environment. *Comput. Sci. Eng.* **9**, 90-95 (2007).

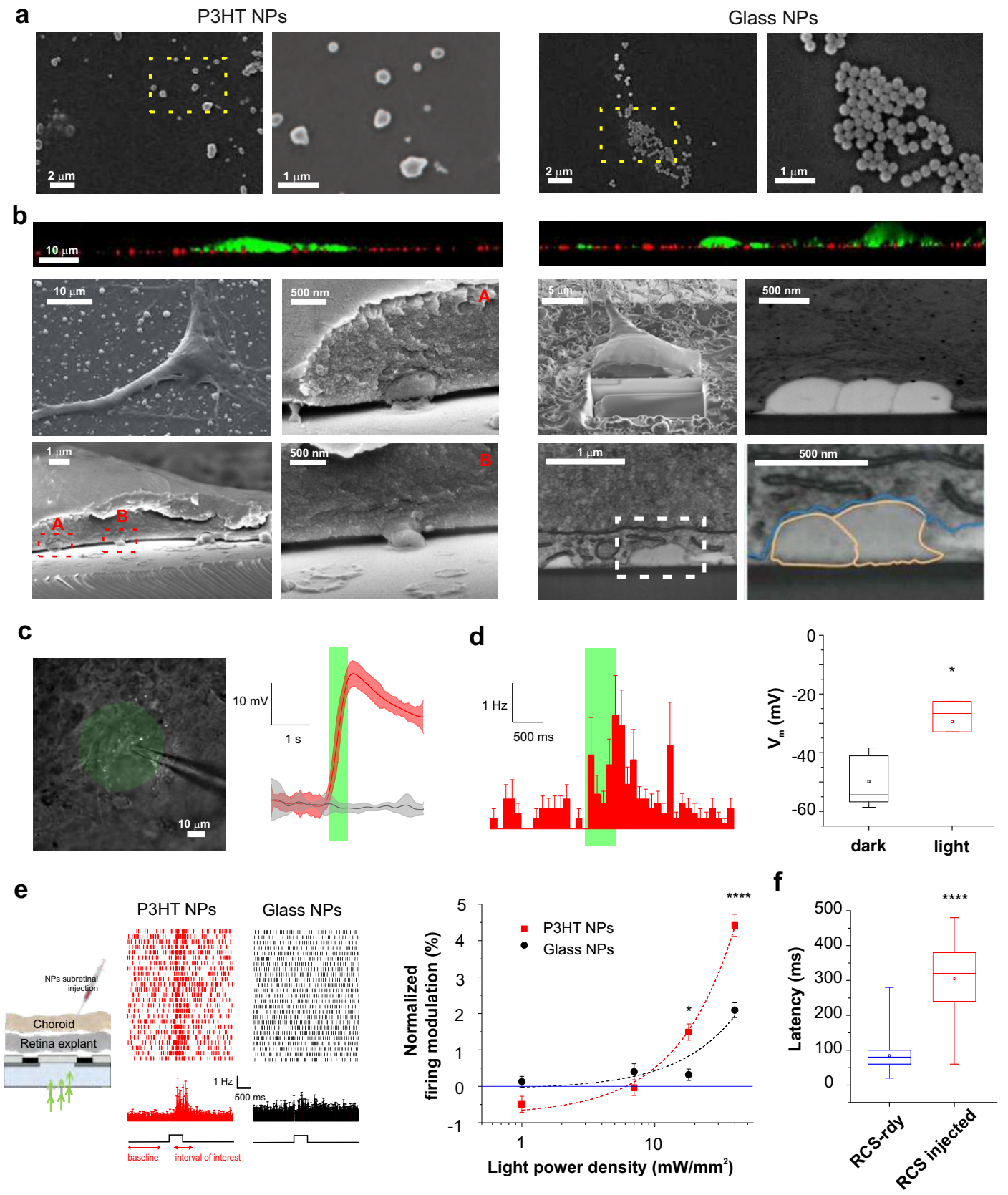
a
P3HT NPs
Glass NPs
2 µm
1 µm
2 µm
1 µm
b
10 µm
10 µm
500 nm
A
5 µm
500 nm
1 µm
A
B
500 nm
B
1 µm
500 nm
c
10 µm
10 mV
1 s
d
1 Hz
500 ms
0
-20
-40
-60
V_m (mV)
*
dark
light
e
P3HT NPs
Glass NPs
NPs subretinal injection
Choroid
Retina explant
1 Hz
500 ms
baseline
interval of interest
P3HT NPs
Glass NPs
****
*
Normalized firing modulation (%)
Light power density (mW/mm²)
f
****
Latency (ms)
RCS-rdy
RCS injected
g
Δ
I_gen
1 F
R_gen
R_m,j
C_m,j
V_m
R_m,ej
C_m,ej
V_m
R_coupling
R_cle
R_el
I_cle
h
V_m modulation (mV)
-69.999
-70.000
-70.001
45 50 55 60
Junctional
Extrajunctional
Time (ms)
Junctional
Extrajunctional
Peak variation (V)
Cleft resistance (Ohm)

FIGURE 1

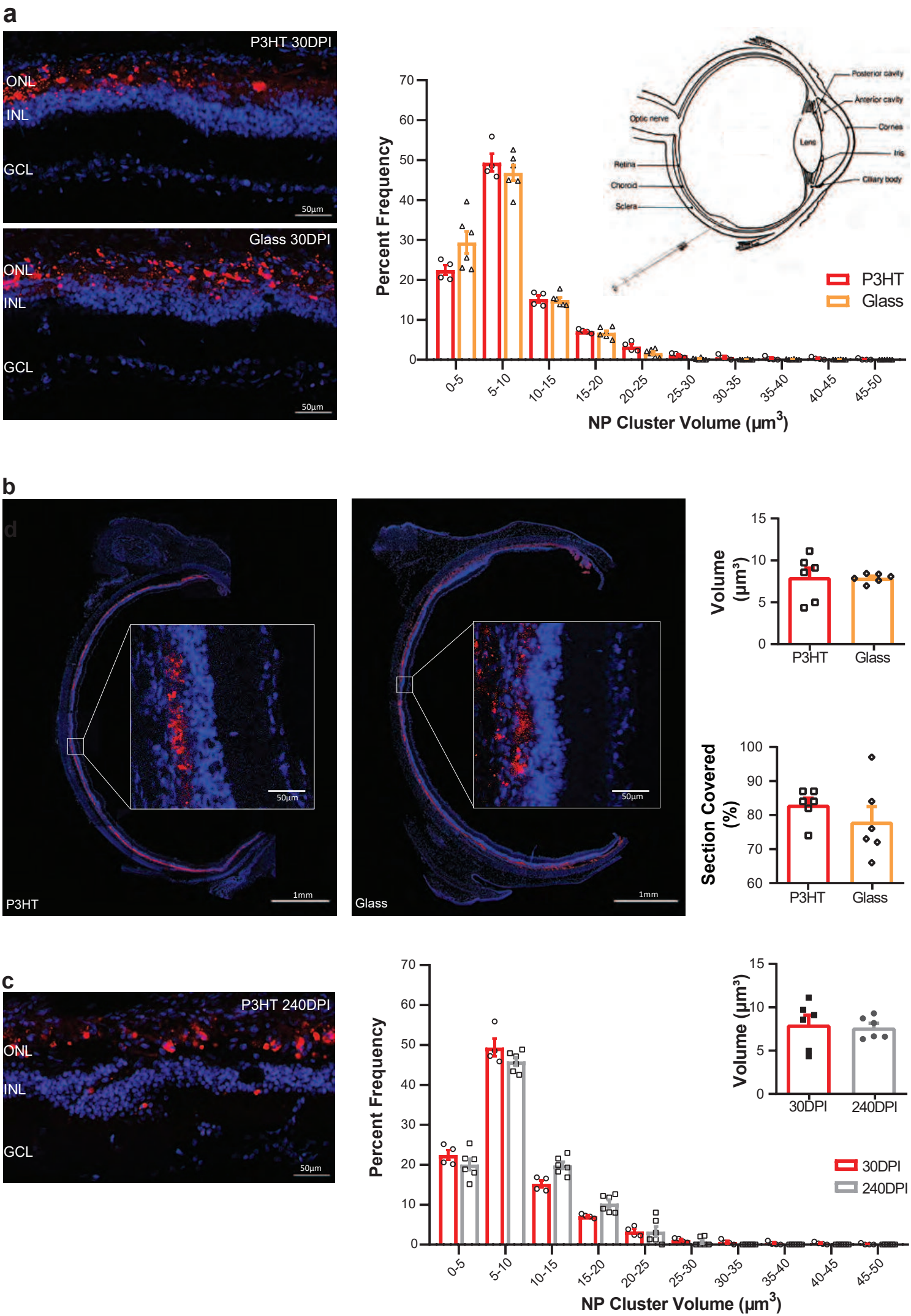
a
P3HT 30DPI
ONL
INL
GCL
50µm
Glass 30DPI
ONL
INL
GCL
50µm
Percent Frequency
70
60
50
40
30
20
10
0
0-5
5-10
10-15
15-20
20-25
25-30
30-35
35-40
40-45
45-50
NP Cluster Volume (µm3)
P3HT
Glass
Posterior cavity
Anterior cavity
Optic nerve
Cornea
Lens
Iris
Retina
Choroid
Ciliary body
Sclera
b
d
50µm
1mm
P3HT
50µm
1mm
Glass
Volume (µm3)
15
10
5
0
P3HT
Glass
Section Covered (%)
100
90
80
70
60
P3HT
Glass
c
P3HT 240DPI
ONL
INL
GCL
50µm
Percent Frequency
70
60
50
40
30
20
10
0
0-5
5-10
10-15
15-20
20-25
25-30
30-35
35-40
40-45
45-50
NP Cluster Volume (µm3)
30DPI
240DPI
Volume (µm3)
15
10
5
0
30DPI
240DPI

FIGURE 2

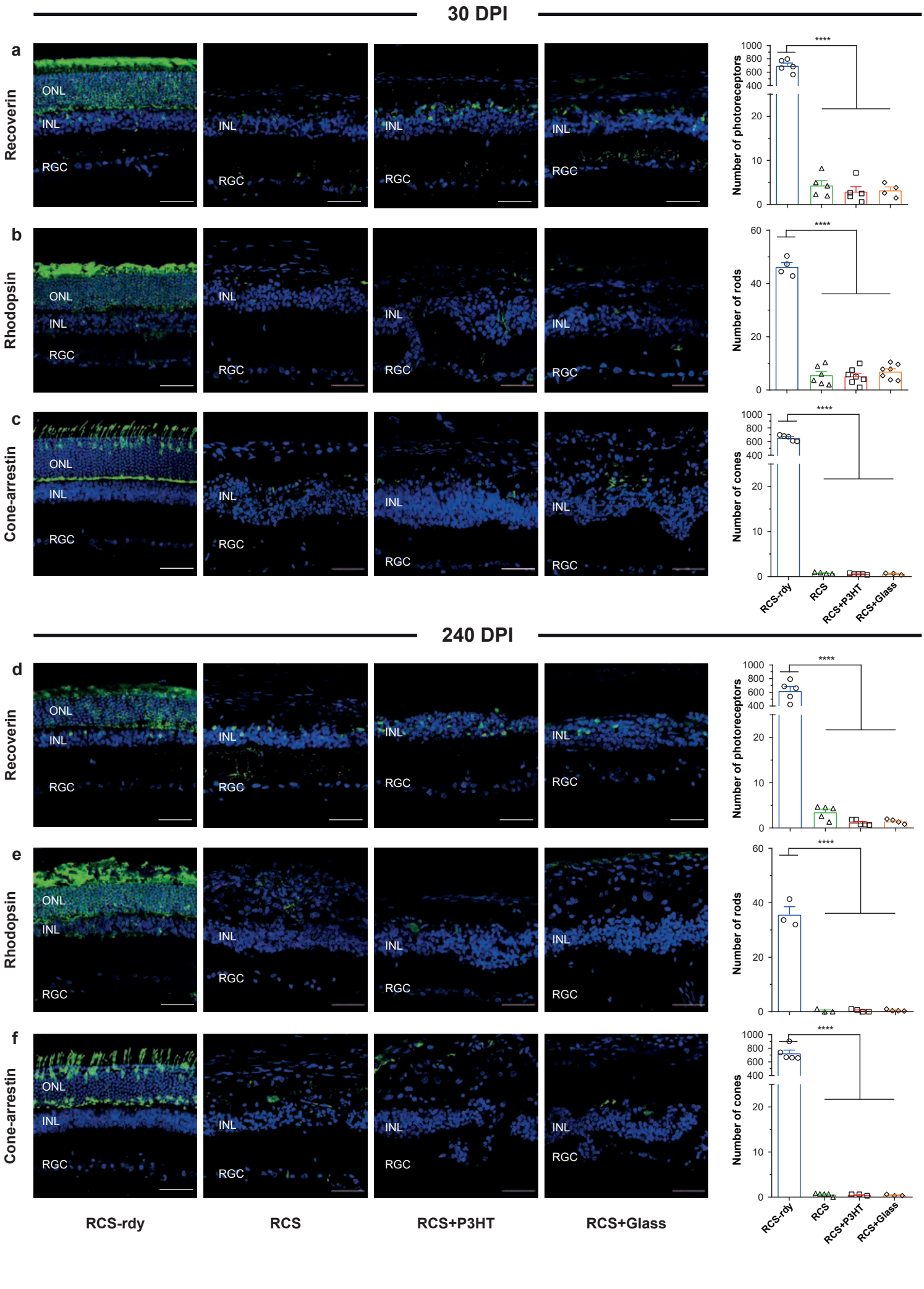
30 DPI
240 DPI
a
b
c
d
e
f
Recoverin
Rhodopsin
Cone-arrestin
ONL
INL
RGC
Number of photoreceptors
Number of rods
Number of cones
****
RCS-rdy
RCS
RCS+P3HT
RCS+Glass

FIGURE 3

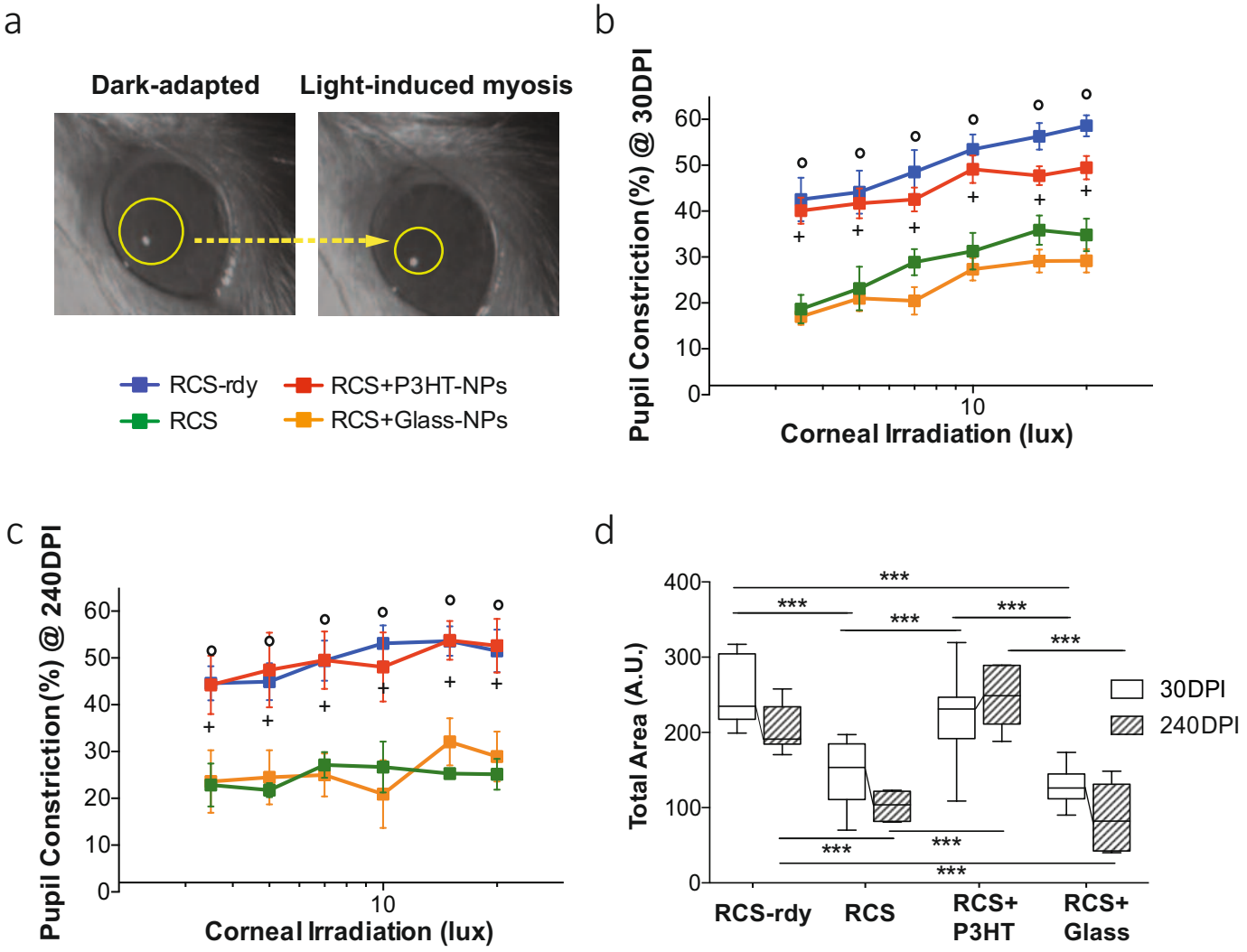
a
Dark-adapted
Light-induced myosis
RCS-rdy
RCS+P3HT-NPs
RCS
RCS+Glass-NPs
b
Pupil Constriction (%) @ 30DPI
Corneal Irradiation (lux)
c
Pupil Constriction (%) @ 240DPI
Corneal Irradiation (lux)
d
Total Area (A.U.)
30DPI
240DPI
RCS-rdy
RCS
RCS+ P3HT
RCS+ Glass

FIGURE 4

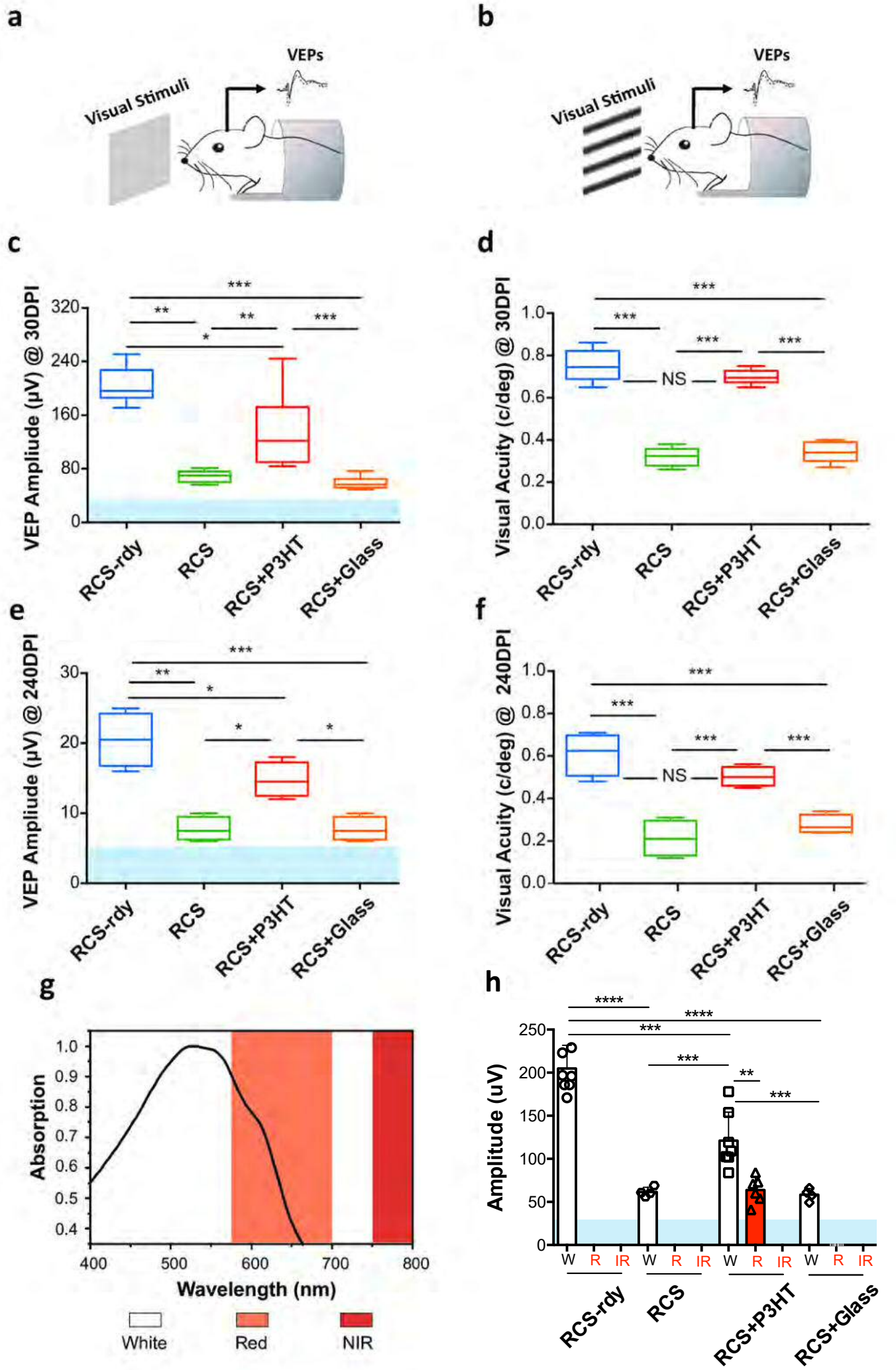
a
VEPs
Visual Stimuli
b
VEPs
Visual Stimuli
c
VEP Ampliude (μV) @ 30DPI
320
240
160
80
0
***
**
**
***
*
RCS-rdy
RCS
RCS+P3HT
RCS+Glass
d
Visual Acuity (c/deg) @ 30DPI
1.0
0.8
0.6
0.4
0.2
0.0
***
***
***
***
NS
RCS-rdy
RCS
RCS+P3HT
RCS+Glass
e
VEP Ampliude (μV) @ 240DPI
30
20
10
0
***
**
*
*
*
RCS-rdy
RCS
RCS+P3HT
RCS+Glass
f
Visual Acuity (c/deg) @ 240DPI
1.0
0.8
0.6
0.4
0.2
0.0
***
***
***
***
NS
RCS-rdy
RCS
RCS+P3HT
RCS+Glass
g
Absorption
1.0
0.9
0.8
0.7
0.6
0.5
0.4
400
500
600
700
800
Wavelength (nm)
White
Red
NIR
h
Amplitude (uV)
250
200
150
100
50
0
****
****
***
***
**
***
W
R
IR
RCS-rdy
RCS
RCS+P3HT
RCS+Glass

FIGURE 5

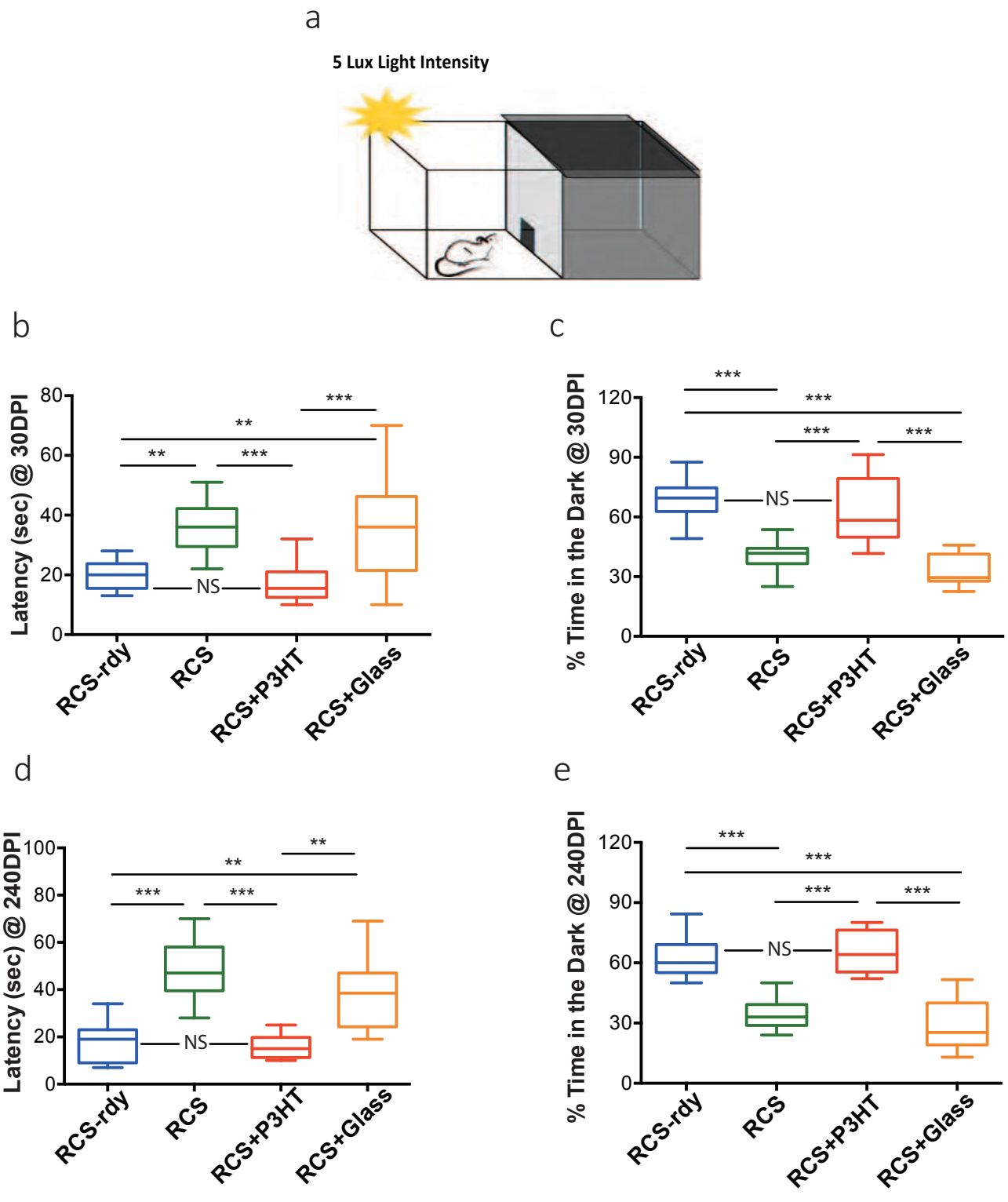
a
5 Lux Light Intensity
b
Latency (sec) @ 30DPI
0
20
40
60
80
**
***
**
***
NS
RCS-rdy
RCS
RCS+P3HT
RCS+Glass
c
% Time in the Dark @ 30DPI
0
30
60
90
120
***
***
***
***
NS
RCS-rdy
RCS
RCS+P3HT
RCS+Glass
d
Latency (sec) @ 240DPI
0
20
40
60
80
100
**
**
***
***
NS
RCS-rdy
RCS
RCS+P3HT
RCS+Glass
e
% Time in the Dark @ 240DPI
0
30
60
90
120
***
***
***
***
NS
RCS-rdy
RCS
RCS+P3HT
RCS+Glass

FIGURE 6